

Intramultiplet mixing in the electron-volt energy range for $\text{Ne}^{**}\{(2p)^5(3p)\}+\text{He}$

W. Boom, R.A.M.L. van Galen, B.J.P. Klaver, S.S. Op de Beek, J.T.A. Heier,
H.C.W. Beijerinck, and B.J. Verhaar

Physics Department, Eindhoven University of Technology, P.O. Box 513, 5600 MB Eindhoven, The Netherlands

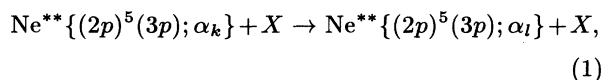
(Received 7 October 1994; revised manuscript received 17 January 1995)

We present measurements on fine-structure-changing $\text{Ne}^{**}\{(2p)^5(3p)\}+\text{He}$ collisions at superthermal energies with an average value of $\langle E \rangle = 470$ meV. For an extensive set of transitions absolute values of polarized-atom cross sections are given. A wide range of cross section magnitudes and polarization effects is observed. Even higher order polarization effects are evidently present. A suitable set of anisotropy parameters is introduced which has large advantages for a direct comparison of experimental and calculated cross sections. Although the experimentally observed polarization effects are reproduced by quantum calculations, the calculated magnitude of the cross section is, in general, larger than the experimental value. Moreover, in contrast with the thermal energy range, the current semiclassical model fails in describing the most prominent cross sections in terms of the “visible” avoided crossings in the adiabatic potentials. In the quantum calculations, clear indications are found for an additional transition mechanism of radial matching. In this mechanism a change in the rotational quantum number of the nuclear motion matches the asymptotic energy gap ΔE_{kl} between the initial and final state k and l , respectively. This process is most efficient at large internuclear distances, thus enhancing the magnitude of the cross section considerably. Radial matching is most effective when $\langle E \rangle / \Delta E_{kl} \gg 1$. The calculated magnitude of the cross section is thus sensitive to details of the long-range part of the potentials used as input. At thermal energies this sensitivity is masked, which explains the good agreement of the calculations with the model potentials of Hennecart and Masnou-Seeuws [J. Phys. B **18**, 657 (1985)] with the experiments in the thermal range.

PACS number(s): 34.50.Pi, 34.50.Rk, 31.50.+w

I. INTRODUCTION

In recent years there is a growing interest in inelastic collisions of short-lived electronically excited states [1–16]. In our crossed beam experiment [17, 18] we study the collision-induced intramultiplet mixing process



with X a rare-gas atom or a small molecule. The different fine-structure levels $\{\alpha\}$ of the $\text{Ne}^{**}\{(2p)^5(3p)\}$ multiplet are denoted by their Paschen numbers k and l , respectively. These short-lived Ne^{**} states (typically $\tau=20$ ns) are produced by laser excitation from the metastable levels 3P_0 or 3P_2 of the $\text{Ne}^*\{(2p)^5(3s)\}$ multiplet. By measuring the fluorescence intensity of a decay mode for both the initial and final state for different laser polarizations, polarized-atom cross sections $Q_{l \leftarrow k}^{|M_k|}$ for the $\{\alpha_k\} \rightarrow \{\alpha_l\}$ transition can be determined. Here $|M_k|$ is the magnetic quantum number of the electronic angular momentum \mathbf{J}_k of the initial $\{\alpha_k\}$ state with respect to the asymptotic relative velocity \mathbf{g} . By calibration of the secondary beam density, absolute values of Q are obtained [19]. By comparing the experimental results with either fully quantum-mechanical coupled-channel calculations [20] or semiclassical calculations [21], detailed insight into the collision dynamics of process Eq. (1) can be obtained.

Recently, a hollow cathode arc (HCA) source [22] for metastable $\text{Ne}^*(^3P_0, ^3P_2)$ atoms has been installed,

supplementing the thermal metastable atom source [23] (TMS). Typical translational energies are in the superthermal range 300–6000 meV for the HCA source, and only 60–170 meV for the TMS. In the center-of-mass frame, collision energy ranges of 200–1200 meV and 50–100 meV, respectively, can be probed for the $\text{Ne}^{**}\text{-He}$ system. The prospect of the HCA source, with an average collision energy of $\langle E \rangle = 470$ meV for $\text{Ne}^{**}\text{-He}$, is to study the process of Eq. (1) at collision energies well above the typical energy splittings between the various fine-structure levels of the Ne^{**} multiplet, ranging from $\Delta E_{k,k+1} = 7$ to 240 meV. The total energy spread of the multiplet is $\Delta E_{1,10} = 584$ meV, although most levels are confined to a smaller interval $\Delta E_{2,9} = 171$ meV. Threshold effects in the thermal energy range result in large polarization effects, e.g., $Q^{0|}/Q^{1|} = 8.9$ for the $\{\alpha_7\} \rightarrow \{\alpha_5\}$ transition with $\Delta E_{5,7} = 81$ meV at a collision energy $\langle E \rangle = 100$ meV [21]. Whether any polarization effect at all is present in the superthermal energy range is yet unclear. For the process of Penning ionization involving $\text{Ne}^{**}\{J_k = 3\}$ atoms effects of the order of $Q^{0|}/Q^{1|} \approx 2$ and 1.5 have been observed in the thermal [24] and the superthermal energy range [25], respectively.

From a theoretical point of view, the broad energy range accessed by the combination of the HCA source and the TMS, provides a rigorous test for the model potentials [1, 2, 20, 26] used as input for our coupled-channel calculations. Moreover, the validity of our semiclassical description of the collision dynamics can be verified in a broader context. The semiclassical model is based upon

localized Landau-Zener type transitions at avoided crossings between different pairs of adiabatic potential curves and a locking radius to switch between a space-fixed and a body-fixed description [21].

This paper describes the application of the newly installed HCA source to experiments for the $\text{Ne}^{**}\text{-He}$ system. A brief overview of the experiment is given in Sec. II A, including the measuring routine, data analysis, and a discussion of systematic errors. The use of anisotropy parameters for the cross section is addressed in Sec. III. In Sec. IV the measurements in the superthermal energy range for the $\text{Ne}^{**}\text{-He}$ system are presented and compared to the results of fully quantum-mechanical coupled-channel calculations. Though in qualitative agreement, the calculated quantum results for the magnitude of the cross section are in general larger than the experimentally obtained values. The most prominent cross sections cannot be understood in the framework of the current semi-classical model (Sec. V). A possible additional transition mechanism, so-called radial matching, is briefly depicted in Sec. VI. This involves a change in rotational quantum number at large internuclear distances and thus assigns the observed differences between the experimental values and the quantum results to possible deficiencies in the long-range part of the model potentials of Hennecart and Masnou-Seeuws [1, 2].

II. EXPERIMENT

A. General setup

The experimental apparatus is described in full detail by Manders *et al.* [18] and Boom [27], so we only briefly discuss it here. In Fig. 1 a schematic overview of the crossed beam apparatus is given, including the newly installed HCA [22].

The scattering center is defined by the intersection of the laser beam and the primary beam of metastable neon atoms. Collision partners are provided by a secondary beam, formed by a skimmerless supersonic expansion emerging from a nozzle, positioned 2 mm below the scattering center. Fluorescence from the decay of the initial, laser-excited state or from a final state populated through a collision-induced transition is monitored. The optical detection system consists of a parabolic mirror for efficient photon collection (solid angle efficiency 40%), selectable narrow-band interference filters for wavelength selection [2 nm full width at half maximum (FWHM), 10 nm FW 10^{-6} M], and a photomultiplier-amplifier combination, operating in pulse counting mode. The total detection efficiency η is about 2×10^{-3} per emitted photon (including branching ratio A_{ki}/A_k of Einstein coefficients) at a wavelength $\lambda=650$ nm.

The laser setup consists of a cw single mode ring dye laser, stabilized in a separate, saturated absorption experiment, with a waist radius $w_l = 0.53$ mm in the scattering center. The linear polarization of the laser is defined by a polarization prism and can be rotated by a $\lambda/2$ retardation plate. The angle β between laser polarization and asymptotic relative velocity \mathbf{g} is relevant for the polarization effect.

The major difference between the HCA source and the TMS is the much larger distance (599 mm for the HCA, 90 mm for the TMS) from source to scattering center, due to geometrical limitations and a higher demand on differential pumping for the HCA source with its larger gas flow of approximately 1 Torr l/s. The geometrical loss factor of 120 is partly compensated, both by the higher center line intensity of the primary beam source and the longer “life path” $l_{\tau}^{c.m.} = g\tau$ of the short-lived Ne^{**} atoms in the center of mass (c.m.) frame. A net loss factor of 12 results for the collision-induced fluorescence. From the performance of $1 \text{ kHz}/\text{\AA}^2$ for the thermal metastable source [18] a performance of $0.08 \text{ kHz}/\text{\AA}^2$ is expected for the HCA source. Initially, however, a background signal of about 6 kHz is found, by far surmounting any collision-induced fluorescence signal. By carefully shielding the source, the background signal due to the continuum blackbody radiation from the hot plasma inside the tungsten hollow cathode is reduced to only 200 Hz.

B. Measuring routine and data analysis

In a basic cross section measurement, both the intensities for collision-induced fluorescence L and direct

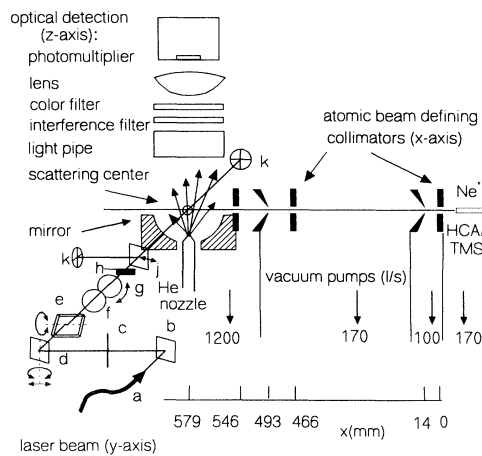


FIG. 1. Schematic view of the crossed beam apparatus, with the Ne^* atomic beam axis (x), the exciting laser beam (y), and the optical detection system and He secondary beam (z). The Ne^* primary beam emerges from the HCA source or TMS through a defining anode of 1 mm diameter and an aperture of 0.7 mm diameter. The He secondary beam emerges from a $50\text{-}\mu\text{m}$ -diam nozzle orifice, positioned 2 mm below scattering center. The laser beam passes the components: (a) optical fiber exit; (b) beam splitter; (c) $f=2$ m lens; (d) translator-rotator module for horizontal alignment laser beam; (e) parallel plate for vertical alignment; (f) polarizer; (g) polarization rotator; (h) laser shutter and iris diaphragm; (j) translatable to switch between quadrant diodes for laser beam alignment; (k) quadrant diodes, spatial reference for laser beam. The origin of the xyz coordinate frame is chosen at the nozzle exit. Pumping speeds for the different vacuum chambers along the primary beam axis are indicated.

fluorescence K are measured [Eq. (1)], with the secondary beam set either “on” or “off.” To correct for stray light from the laser each of these intensities is measured both with the laser on resonance (frequency ν_0) and detuned (frequency $\nu_0 + \Delta\nu$) by $\Delta\nu = 80$ MHz. The ratio between the “net” collision-induced and direct fluorescence signals I_l/I_k is now simply given by [18]

$$\left[\frac{I_l}{I_k} \right]_{\text{expt}} = \frac{L^{\text{on}}}{K^{\text{on}}} - \frac{L^{\text{off}}}{K^{\text{off}}}, \quad (2)$$

$$L^{\text{on}} = L^{\text{on}}(\nu_0) - L^{\text{on}}(\nu_0 + \Delta\nu),$$

in which the second term corrects for the “leakage” of direct fluorescence through the filters used for collision-induced fluorescence.

A complete polarization measurement typically consists of a series of 15 cross section measurements, equally distributed over a 180° interval of the angle β between laser polarization and relative velocity. All direct fluorescence signals K are measured at a single angle β . Since $L^{\text{off}}/K^{\text{off}}$ is usually comparable to its statistical error or at most a few percent of $L^{\text{on}}/K^{\text{on}}$ corresponding intensities are only measured at a single angle β before and after the complete polarization measurement. This roughly saves a factor 2 in measuring time. Depending upon the actual signals, a complete polarization measurement over 180° takes about 40 to 90 minutes.

A numerical simulation [28] of the experiment takes into account the finite size of the scattering center, the spread in the velocity distributions, and the details of the optical pumping process. From this simulation a convolution factor ξ is determined, relating the actual ratio I_l/I_k of collision-induced and direct fluorescence signals to the first order expression $[I_l/I_k]_{\text{ideal}}$ by

$$\left[\frac{I_l}{I_k} \right] = \xi \left[\frac{I_l}{I_k} \right]_{\text{ideal}} = \xi \left[\frac{\eta_l}{\eta_k} \right]_0 n_2 l_\tau^{c.m.} Q_{l \leftarrow k}(g). \quad (3)$$

The subscript “ideal” refers to a point-size scattering center and disregards the velocity spread. Supersonic expansion theory [19] is used to calculate the secondary beam density n_2 . Further, $Q_{l \leftarrow k}(g)$ is the desired cross section for the $\{\alpha_k\} \rightarrow \{\alpha_l\}$ transition at relative velocity g and $l_\tau^{c.m.} = g\tau$ the life path in the center-of-mass system. The optical detection efficiencies η_l and η_k are taken at the optical axis for convenience, but all other quantities, such as the secondary beam density n_2 , are evaluated at the position $(x_{\text{SC}}, z_{\text{SC}})$ of the scattering center. The difference between the position x_l of the laser beam and the average position x_{SC} of the collision-induced fluorescence is taken from a Monte Carlo simulation [28] of the optical excitation process. Typical values are $(x_{\text{SC}} - x_l) = -0.2$ mm and $(z_{\text{SC}} - z_l) = -0.03$ mm, i.e., the excitation occurs more in the upstream wing of the laser beam and the scattering events are shifted slightly to the higher density region closer to the nozzle.

Due to the broad velocity distribution of the HCA source, the convolution factor ξ strongly depends on the assumed velocity dependency of the total cross section. For example, it varies between 0.90 and 1.14 for energy dependencies of the cross section $Q \sim 1/g$ and $Q \sim g$,

respectively. Since no experimental information on the energy dependency is available, we do not apply the correction factor and take $\xi = 1.00$ for clarity. Concluding, an additional 12% uncertainty in the absolute value of the cross section results from this process of convolution.

C. Systematic errors

The optimum operating pressure for the secondary beam is given by the condition of a $1/e$ attenuation of the primary beam of metastable neon atoms before it reaches the laser beam at the scattering center, as discussed by Manders *et al.* [18]. The attenuation of the beam of short-lived $\text{Ne}^{**}\{\alpha_k\}$ atoms is only 4% for an assumed (large) cross section $Q = 100 \text{ \AA}^2$, as follows from a typical value $n_2 l_\tau^{\text{lab}} = v_1 \tau$ of the secondary beam density $n_2 = 4 \times 10^{20} \text{ m}^{-3}$ and the life path $l_\tau^{\text{lab}} = 100 \text{ \mu m}$ in the laboratory system at $v_1 = 5000 \text{ m/s}$. The influence of depolarizing collisions *before* the inelastic transition and additional fine-structure-changing collisions *after* the inelastic transition considered is thus negligible. This has also been checked by varying the secondary beam operating pressure [18]. The $\text{Ne}^{**}\{\alpha_k\}$ collisions are thus investigated at near ideal single collision conditions, in spite of the large attenuation of the beam of metastable atoms upstream of the scattering center.

There are three major systematic errors in the experimental results for the magnitude of the cross section. First, the alignment of the primary beam with respect to the nozzle orifice (accuracy 0.1 mm) results in a systematic error of 5%. Second, the calibration of the detection efficiency η_l at the wavelength of the collision-induced fluorescence of the final state relative to its value at the wavelength of the direct fluorescence η_k of the initial state results in an estimated systematic error of 5%. Third, there is the effect of the velocity dependence of the cross section on the convolution factor ξ , resulting in a systematic error of 12% as discussed above. The total systematic error, obtained by adding these three error bars, is 22% in the superthermal energy range as presented in this paper. In comparison, the error in the Einstein A coefficients is negligible.

For the experimental results in the thermal energy range, as presented by Manders *et al.* [20, 21], the systematic error is estimated at only 14% due to the much better determined value of the collision energy of the TMS.

III. POLARIZED-ATOM CROSS SECTIONS

The experimental cross section $Q_{l \leftarrow k}^\beta$ as a function of the angle β between \mathbf{g} and the optical quantization axis is given by

$$Q_{l \leftarrow k}^\beta = \sum_{n=0}^{J_k} J_k C_{2n} \cos(2n\beta). \quad (4)$$

In more detail [20],

$$Q_{l \leftarrow k}^\beta = \sum_{m_k=-J_k}^{J_k} w_{m_k} \sum_{M_k=-J_k}^{J_k} \{d_{m_k M_k}^{J_k}(\beta)\}^2 Q_{l \leftarrow k}^{|M_k|}. \quad (5)$$

In this expression, M_k and m_k are the magnetic quantum numbers of J_k along \mathbf{g} and the optical quantization axis, respectively. The first summation adds the contributions for the various magnetic substates m_k that have been excited with a relative population w_{m_k} in the optical pumping process. The second summation is due to the transformation from the optical quantization axis to \mathbf{g} as the relevant quantization axis for the collision process, using reduced Wigner functions $d_{m_k M_k}^{J_k}(\beta)$.

Though the coefficients ${}^{J_k}C_{2n}$ most closely relate to the net polarization effect observed in $Q_{l\leftarrow k}^\beta$, both the effects of differing $Q_{l\leftarrow k}^{|M_k|}$ values and the (uninteresting) w_{m_k} distribution are present. The values for $Q_{l\leftarrow k}^{|M_k|}$ in their turn can be compared directly to the coupled-channel quantum calculations, but are not a direct representation of the net polarization effect. An alternative data representation for the cross section is the anisotropy parameters \mathcal{P} , \mathcal{Q} , \mathcal{R} , given by

$$\begin{aligned}\mathcal{P} &= (Q_{l\leftarrow k}^{|0|} - Q_{l\leftarrow k}^{|1|})/Q_{l\leftarrow k}, \\ \mathcal{Q} &= (3Q_{l\leftarrow k}^{|0|} - 4Q_{l\leftarrow k}^{|1|} + Q_{l\leftarrow k}^{|2|})/4Q_{l\leftarrow k}, \\ \mathcal{R} &= (-10Q_{l\leftarrow k}^{|0|} + 15Q_{l\leftarrow k}^{|1|} - 6Q_{l\leftarrow k}^{|2|} + Q_{l\leftarrow k}^{|3|})/16Q_{l\leftarrow k},\end{aligned}\quad (6)$$

in which $Q_{l\leftarrow k}$ is the unpolarized cross section

$$Q_{l\leftarrow k} = \frac{1}{2J_k + 1} \sum_{M_k=-J_k}^{J_k} Q_{l\leftarrow k}^{|M_k|} \quad (7)$$

and \mathcal{P} , \mathcal{Q} , \mathcal{R} are each normalized in the sense that the sum over the absolute values of their coefficients in Eq. (6) equals unity. The choice for \mathcal{P} , \mathcal{Q} , \mathcal{R} in Eq. (6) is inspired by the expansion of the initial diagonal density matrix $\rho_{m'_k m_k} = w_{m_k} \delta_{m'_k m_k}$ in the $m'_k m_k$ representation in irreducible spherical tensor parts [29].

Without any assumption on the excitation process we find the following relations between the ${}^{J_k}C_{2n}$ coefficients

(relating directly to the observed polarization effect) and the anisotropy parameters \mathcal{P} , \mathcal{Q} , and \mathcal{R} :

$${}^{J_k}C_{2n} = [\delta_{2n,0} + \mathbf{w} \cdot (\mathbf{c}_P \mathcal{P} + \mathbf{c}_Q \mathcal{Q} + \mathbf{c}_R \mathcal{R})] Q_{l\leftarrow k}, \quad (8)$$

with $\mathbf{w} = (w_{m_k=-J_k}, \dots, w_{m_k=J_k})$. The coefficients \mathbf{c}_P , \mathbf{c}_Q , and \mathbf{c}_R are given in Table I. Equation (8) is the result of geometric symmetry only. The details of the excitation and collision process are split off in separate factors. Though independent of the actual w_{m_k} distribution, the parameters \mathcal{P} , \mathcal{Q} , \mathcal{R} are directly related to the observed polarization effect. For $J_k = 2$, for example, no $\cos(4\beta)$ effect is present when $\mathcal{Q} = 0$, a dominant $\cos(2\beta)$ effect is only present for a specific w_{m_k} -dependent ratio of \mathcal{Q}/\mathcal{P} , and no polarization effect at all is observed when $\mathcal{P} = \mathcal{Q} = 0$.

The coefficients of the \mathcal{P} , \mathcal{Q} , \mathcal{R} terms in Eq. (8) obey the proper limiting cases. For an isotropic w_{m_k} distribution, i.e., the case of no net polarization of the atom, each coefficient of \mathcal{P} , \mathcal{Q} , and \mathcal{R} vanishes. The only nonzero coefficient then is ${}^{J_k}C_0 = Q_{l\leftarrow k}$.

For the case of the low power limit of the laser excitation process the w_{m_k} distribution is determined by the relative excitation rate, i.e., the squared Clebsch-Gordan coefficient, for the various $m_i \rightarrow m_k$ transitions. In this low power limit, one finds ${}^{J_k}C_{2n} = 0$ for $n \geq 2$, for both a linear and a circular laser polarization. Only the constant term ${}^{J_k}C_0$ and the lowest order ${}^{J_k}C_2$ coefficient of the $\cos(2\beta)$ polarization effect are nonvanishing. This directly reflects the dipole character of the optical transition.

Higher order polarization effects can only be observed by deviating from the low power w_{m_k} distribution. Saturation effects, a large branching ratio back to the original level, or the presence of a magnetic field are required for this.

From now on, we restrict ourselves to the case of a linear laser polarization. The following w_{m_k} relations

TABLE I. The coefficient vectors \mathbf{c}_P , \mathbf{c}_Q , and \mathbf{c}_R of Eq. (8) for the relation between the Fourier coefficients ${}^{J_k}C_{2n}$ of the polarized atom cross sections and the anisotropy parameters \mathcal{P} , \mathcal{Q} , and \mathcal{R} .

${}^{J_k}C_{2n}$	\mathbf{c}_P	\mathbf{c}_Q	\mathbf{c}_R
1C_0	$\frac{1}{12}(-1, 2, -1)$	0	0
1C_2	$\frac{1}{4}(-1, 2, -1)$	0	0
2C_0	$\frac{1}{4}(-2, 1, 2, 1, -2)$	$\frac{1}{80}(47, -28, -38, -28, 47)$	0
2C_2	$\frac{3}{4}(-2, 1, 2, 1, -2)$	$\frac{1}{4}(7, -4, -6, -4, 7)$	0
2C_4	0	$\frac{1}{16}(1, -4, 6, -4, 1)$	0
3C_0	$\frac{1}{4}(-5, 0, 3, 4, 3, 0, -5)$	$\frac{1}{16}(61, -9, -33, -38, -33, -9, 61)$	$\frac{1}{224}(593, -142, -289, -324, -289, -142, 593)$
3C_2	$\frac{1}{4}(-15, 0, 9, 12, 9, 0, -15)$	$\frac{5}{4}(9, -1, -5, -6, -5, -1, 9)$	$\frac{1}{64}(495, -90, -255, -300, -255, -90, 495)$
3C_4	0	$\frac{5}{16}(3, -7, 1, 6, 1, -7, 3)$	$\frac{3}{32}(11, -26, 5, 20, 5, -26, 11)$
3C_6	0	0	$\frac{1}{64}(1, -6, 15, -20, 15, -6, 1)$

then apply:

$$\begin{aligned}
 {}^3P_{0,2} \rightarrow J_k & : w_{-m_k} = w_{m_k}, \\
 {}^3P_0 \rightarrow J_k = 1 & : w_0 = 1, w_1 = 0, \\
 {}^3P_2 \rightarrow J_k = 2 & : w_0 = 0, \\
 {}^3P_2 \rightarrow J_k = 3 & : w_3 = 0.
 \end{aligned} \tag{9}$$

The actual w_{m_k} distribution for the $J_k = 2, 3$ initial states is determined in a Monte Carlo simulation [28] of

the laser excitation, taking into account the coherence of the excitation process and the stochastic nature of spontaneous emission. Time integrated results are presented in Table II.

For a specific excitation scheme, the expansions of $J_k C_{2n}$ in $\mathcal{P}, \mathcal{Q}, \mathcal{R}$ terms provide a natural way to determine if higher order polarization effects are likely to be revealed experimentally. As an example, we now discuss the $J_k = 3$ case in more detail. Substituting the values of Table II in Eq. (8) we find

$$\begin{aligned}
 J_k = 3 : Q_{l \leftarrow 9}^\beta / Q_{l \leftarrow 9} &= 1 + 0.74(\mathcal{P} - 2.66\mathcal{Q} - 1.70\mathcal{R}) + 2.22(\mathcal{P} - 2.72\mathcal{Q} - 1.75\mathcal{R}) \cos(2\beta) \\
 &+ 0.56(\mathcal{Q} + 1.07\mathcal{R}) \cos(4\beta) - 0.02\mathcal{R} \cos(6\beta).
 \end{aligned} \tag{10}$$

If \mathcal{R} is nonzero, not only is a $\cos(6\beta)$ term present, but a $\cos(4\beta)$ and $\cos(2\beta)$ term are also present, 30 to 200 times larger in amplitude, respectively. Therefore a $\cos(6\beta)$ contribution is unlikely to be “recognized” in the experimental data. A similar argument applies to \mathcal{Q} , now with “only” a factor 12 between the contributing $\cos(4\beta)$ and $\cos(2\beta)$ terms.

As to the comparison between experimental and calculated results, a serious problem now arises. If a higher order $\cos(2n\beta)$ term is not evidently present in the experimental data, this does not imply that the corresponding anisotropy parameter equals zero. It may still be present in the lower order terms. In our data analysis, however, we have to set this parameter to zero. Clearly, this is to prevent a serious error buildup. As a consequence, the experimentally determined anisotropy parameters $\mathcal{P}^{\text{expt}}, \mathcal{Q}^{\text{expt}}, \mathcal{R}^{\text{expt}}$ cannot directly be compared

to their coupled-channel counterparts $\mathcal{P}^{\text{CC}}, \mathcal{Q}^{\text{CC}}, \mathcal{R}^{\text{CC}}$. In most cases though, the expansions of $J_k C_{2n}$ in $\mathcal{P}, \mathcal{Q}, \mathcal{R}$ terms provide a natural way out. For example, for the two extremal w_{m_k} distributions of the $J_k = 2$ cases in Table II, as determined by the Monte Carlo simulation of the laser excitation at the laser power used, we find

$$\begin{aligned}
 J_k = 2 : Q_{l \leftarrow 4}^\beta / Q_{l \leftarrow 4} &= 1 - 0.10(\mathcal{P} - 0.88\mathcal{Q}) \\
 &- 0.31(\mathcal{P} - 0.95\mathcal{Q}) \cos(2\beta) \\
 &- 0.10\mathcal{Q} \cos(4\beta), \\
 J_k = 2 : Q_{l \leftarrow 6}^\beta / Q_{l \leftarrow 6} &= 1 - 0.16(\mathcal{P} - 1.02\mathcal{Q}) \\
 &- 0.49(\mathcal{P} - 1.05\mathcal{Q}) \cos(2\beta) \\
 &- 0.08\mathcal{Q} \cos(4\beta).
 \end{aligned} \tag{11}$$

If no $\cos(4\beta)$ term shows up, we take $\mathcal{Q}^{\text{expt}}=0$. Only two experimental parameters can be determined, i.e., the un-

TABLE II. Time integrated population distribution $w_{m_k} = w_{-m_k}$ over the magnetic sublevels of the initial $\{\alpha_k, J_k\}$ state obtained by a Monte Carlo simulation [28] of the excitation process with a linear polarized laser. The experimental parameters used are laser power $P = 500 \mu\text{W}$, primary beam velocity $v_1 = 5000 \text{ m/s}$, and no magnetic field present (Helmholtz coils to compensate earth magnetic field). For comparison the low and high power limits are also given. Both are determined by squared ratios of Clebsch-Gordan coefficients; the first by the ones giving the relative pumping speed for the various $m_k = m_l$ transitions, the second by the ones corresponding to $m_k \neq m_l$ population exchanges by spontaneous emission.

Initial state	J_k	w_0	w_1	w_2
$\{\alpha_4\}$	2	0	0.265	0.235
$\{\alpha_6\}$	2	0	0.225	0.275
$\{\alpha_8\}$	2	0	0.235	0.265
Low power limit	2	0	0.1 ($=\frac{1}{10}$)	0.4 ($=\frac{2}{5}$)
High power limit	2	0	0.25 ($=\frac{1}{4}$)	0.25 ($=\frac{1}{4}$)
$\{\alpha_9\}$	3	0.38	0.24	0.07
Low power limit	3	0.257 ($=\frac{9}{35}$)	0.229 ($=\frac{8}{35}$)	0.143 ($=\frac{1}{7}$)
High power limit	3	0.476 ($=\frac{10}{21}$)	0.238 ($=\frac{5}{21}$)	0.024 ($=\frac{1}{42}$)

polarized cross section $Q_{l \leftarrow k}$ and an effective experimental anisotropy parameter $\mathcal{P}^{\text{expt}}$. Our coupled-channel code, however, provides all three parameters $Q_{l \leftarrow k}^{\text{CC}}$, \mathcal{P}^{CC} , and Q^{CC} .

For the first example given in Eq. (11), the effective experimental parameter $\mathcal{P}^{\text{expt}}$, determined by taking $Q^{\text{expt}}=0$, in fact represents $(\mathcal{P} - 0.95Q) \approx (\mathcal{P} - 0.88Q)$. In general for $J_k=2$, when no $\cos(4\beta)$ term shows up, we choose to compare

$$J_k = 2, Q^{\text{expt}} = 0 : \mathcal{P}^{\text{expt}} \iff (\mathcal{P} - Q)^{\text{CC}}. \quad (12)$$

Similarly, after rewriting Eq. (10) for the $J_k = 3$ case, if no $\cos(6\beta)$ term shows up, we choose to compare

$$J_k = 3, \mathcal{R}^{\text{expt}} = 0 : \begin{aligned} \mathcal{P}^{\text{expt}} &\iff (\mathcal{P} + \mathcal{R})^{\text{CC}} \\ Q^{\text{expt}} &\iff (Q + \mathcal{R})^{\text{CC}}. \end{aligned} \quad (13)$$

If only a $\cos(2\beta)$ term is present for $J_k = 3$, we choose to compare

$$J_k = 3, \mathcal{R}^{\text{expt}} = Q^{\text{expt}} = 0 : \mathcal{P}^{\text{expt}} \iff (\mathcal{P} - 2.7Q - 1.8\mathcal{R})^{\text{CC}}. \quad (14)$$

The latter expression can also be written as $\simeq (\mathcal{P} + \mathcal{R})^{\text{CC}} - 2.8(Q + \mathcal{R})^{\text{CC}}$, which directly relates to the terms in Eq. (14).

Finally we like to stress that a careful numerical (or experimental) determination of the w_{m_k} distribution is important for a correct data analysis. Although the extremal w_{m_k} distributions for $J_k = 2$ only differ slightly, the corresponding coefficients of $(\mathcal{P} - Q)$ in Eq. (11) differ by a factor 1.6. For $J_k = 3$ the seemingly small deviation of the w_{m_k} distribution from the high power limit corresponds to a reduction of the $\cos(6\beta)$ and $\cos(4\beta)$ terms to half their values.

Concluding, the anisotropy parameters are highly suitable for representing our experimental and quantum mechanical data. They are directly related to the observed

polarization effects and mostly offer convenient ways to circumvent dependency problems when comparing quantum-mechanical and experimental data with small or negligible higher order polarization effects.

IV. EXPERIMENTAL RESULTS

In a least squares analysis of the experimental data first the coefficients ${}^J_k C_{2n}$ are determined, after which Eq. (8) is used to obtain $\mathcal{P}, Q, \mathcal{R}$.

In Tables III–V experimental cross sections are presented for a set of 29 collision-induced transitions in the $\text{Ne}^{**}\text{-He}$ system, classified by the value of J_k . For the $J_k = 1$ case, formerly measured TMS cross sec-

TABLE III. Experimental and quantum-mechanical anisotropy parameters \mathcal{P} and unpolarized cross sections $Q_{l \leftarrow k}$ for various $\{\alpha_k\} \rightarrow \{\alpha_l\}$ transitions with $J_k = 1$. For comparison the thermal data labelled TMS [20, 21] are also given. Only statistical errors are indicated. The coupled-channel calculations are referred to as ‘‘CC’’ and are labeled (1), (2), and (3) for collision energies $E_{\text{CC}}=350$ meV, $E_{\text{CC}}=525$ meV, and $E_{\text{CC}} = 100$ meV, respectively.

k	l	E_{expt} (meV)	$Q_{l \leftarrow k}$ (\AA^2)	$Q_{l \leftarrow k}^{\text{CC}}/Q_{l \leftarrow k}$		$\mathcal{P}^{\text{expt}}$	\mathcal{P}^{CC}	
				(1)	(2)		(1)	(2)
5	4	500	11.8(1)	1.4	1.4	-0.10(2)	0.04	-0.05
	6	450	4.08(6)	1.0	1.6	-0.60(3)	-0.63	-0.71
	7	460	2.12(3)	2.3	2.0	0.81(4)	1.06	0.76
	8	450	1.42(2)	1.4	1.6	0.67(5)	0.90	0.91
	9	450	1.52(2)	1.1	1.5	0.86(5)	0.73	0.84
7	4	470	3.40(3)	1.2	1.3	-0.56(1)	-0.62	-0.41
	5	500	2.02(5)	1.8	1.8	1.20(7)	1.50	1.15
	6	500	11.9(2)	1.6	1.8	-0.19(5)	-0.54	-0.21
TMS								
(3)								
5	4	100	12.7	1.1		0.05	0.05	
	6	100	0.8	1.0		-0.58	-0.32	
	7	100	3.7	1.0		1.36	1.43	
7	4	140	1.0	1.0		-0.85	-0.86	
	5	140	1.1	0.9		2.0	2.1	
	6	140	5.5	1.3		-0.95	-1.1	

TABLE IV. Experimental and quantum-mechanical anisotropy parameters \mathcal{P} , \mathcal{Q} , and unpolarized cross sections $Q_{l\leftarrow k}$ for various $\{\alpha_k\} \rightarrow \{\alpha_l\}$ transitions with $J_k = 2$. Statistical errors only are indicated. The coupled-channel calculations are referred to as “CC” and are labeled (1) and (2) for collision energies $E_{CC}=350$ meV and $E_{CC}=525$ meV, respectively. In the data analysis we assumed $Q^{\text{expt}} = 0$, and the effective parameter $\mathcal{P}^{\text{expt}}$ is to be compared with $(\mathcal{P} - \mathcal{Q})^{\text{CC}}$.

k	l	E_{expt} (meV)	$Q_{l\leftarrow k}$ (\AA^2)	$Q_{l\leftarrow k}^{\text{CC}}/Q_{l\leftarrow k}$		$\mathcal{P}^{\text{expt}}$	$(\mathcal{P} - \mathcal{Q})^{\text{CC}}$		\mathcal{Q}^{CC}	
				(1)	(2)		(1)	(2)	(1)	(2)
4	6	430	2.58(3)	1.6	2.3	-0.31(4)	-0.09	-0.07	0.20	0.51
	7	430	1.53(2)	2.2	2.1	-0.10(5)	0.01	-0.02	-0.21	-0.14
	8	430	1.02(1)	1.4	1.6	0.37(4)	0.28	0.27	0.90	0.70
	9	430	1.12(2)	1.3	1.5	0.07(7)	0.02	-0.04	-0.37	-0.33
6	4	450	3.28(3)	0.8	1.4	0.13(2)	0.12	0.13	0.52	0.36
	5	450	1.86(2)	0.8	1.7	-0.17(3)	-0.09	-0.18	-0.53	-0.23
	7	450	6.95(6)	1.7	1.9	-0.04(2)	0.00	-0.08	-0.23	-0.14
	8	450	3.41(3)	1.1	1.5	0.23(2)	0.18	0.16	0.34	0.29
	9	450	2.51(2)	1.2	1.1	0.19(2)	0.12	0.04	-0.26	-0.21
8	4	490	0.867(6)	1.0	1.3	0.34(1)	0.29	0.41	0.23	0.91
	5	490	0.564(8)	1.0	1.8	-0.06(4)	-0.07	-0.09	-1.39	-1.08
	6	490	2.26(2)	1.3	1.9	0.14(3)	0.16	0.31	0.17	0.52
	7	500	4.63(4)	1.6	1.7	0.05(2)	0.16	0.07	0.27	-0.02
	9	500	19.1(1)	1.6	1.7	-0.13(2)	-0.13	-0.08	-0.12	-0.24
	10	500	2.00(2)	0.5	0.5	-0.15(4)	-0.14	-0.12	-0.32	-0.30

tions are also given [20, 21]. Furthermore, quantum-mechanical coupled-channel results are presented for 100 meV ($J_k = 1$ only), 350 meV, and 525 meV. The first energy corresponds to the TMS source, the latter two roughly span the energy range accessed by the HCA source. Full polarization measurements are only given for a representative subset in Figs. 2–6. In this section we describe the main features of this data set and compare experimental and quantum results.

A wide spectrum of cross section magnitudes and polarization effects is observed. Magnitudes range from 0.2 to 20 \AA^2 for the $\{\alpha_9\} \rightarrow \{\alpha_5\}$ and $\{\alpha_8\} \rightarrow \{\alpha_9\}$ transition (Figs. 5 and 6), respectively, anisotropy parameters for the polarization effect from $\mathcal{P} = -0.60$ to $\mathcal{P} = 1.2$ for the $\{\alpha_5\} \rightarrow \{\alpha_6\}$ and $\{\alpha_7\} \rightarrow \{\alpha_5\}$ transition (Figs. 2 and 3), respectively.

Due to the large primary beam velocity v_1 with respect to the secondary beam velocity v_2 , the relative velocity \mathbf{g} is mainly determined by \mathbf{v}_1 and the spread in the angle β between laser polarization and \mathbf{g} is limited, allowing well resolved measurements of polarization effects in the cross section. On the other hand, these cross sections are averaged over the relative velocity distribution.

A. Initial state $J_k = 1$

The most pronounced polarization effects are observed for the $\{\alpha_5\}$ and $\{\alpha_7\}$ initial states with $J_k=1$, as depicted in Figs. (2) and (3). These pronounced effects are essentially due to the fact that only the $m_k = 0$ level is populated in the excitation process. The extrema

TABLE V. Experimental and quantum-mechanical data for various $\{\alpha_9\} \rightarrow \{\alpha_l\}$ transitions with $J_k = 3$. Statistical errors only are indicated. The coupled-channel calculations are referred to as “CC” and are labeled (1) and (2) for collision energies $E_{CC}=350$ meV and $E_{CC}=525$ meV, respectively. In the data analysis we assumed $\mathcal{R}^{\text{expt}} = \mathcal{Q}^{\text{expt}} = 0$, and the effective parameter $\mathcal{P}^{\text{expt}}$ is to be compared with $(\mathcal{P} - 2.7\mathcal{Q} - 1.8\mathcal{R})^{\text{CC}}$.

k	l	E_{expt} (meV)	$Q_{l\leftarrow k}$ (\AA^2)	$Q_{l\leftarrow k}^{\text{CC}}/Q_{l\leftarrow k}$		$\mathcal{P}^{\text{expt}}$	$(\mathcal{P} - 2.7\mathcal{Q} - 1.8\mathcal{R})^{\text{CC}}$	
				(1)	(2)		(1)	(2)
9	4	450	0.268(5)	1.7	2.8	0.15(1)	0.22	0.16
	5	450	0.255(2)	1.3	2.3	0.153(7)	0.23	0.24
	6	450	0.76(1)	1.8	2.1	0.10(1)	0.13	0.12
	7	450	1.82(2)	1.8	2.7	0.116(6)	0.15	0.13
	8	450	8.5(1)	2.4	2.6	0.009(9)	0.01	-0.01
	10	450	1.39(2)	0.9	0.6	0.065(7)	0.049	0.067

in $Q_{l \leftarrow k}^\beta$ directly correspond to the pure M_k state cross sections $Q_{l \leftarrow k}^{|M_k|}$. For each of the initial states the whole range of polarization effects is observed and (almost) a decade in cross section magnitude is spanned. The angle β for the different data points is calculated from the experimentally known orientations of the laser polarization and \mathbf{g} , assuming a point-size scattering center and using averages for v_1 and v_2 . In the data fit a constant offset in β is allowed. In the most recently obtained cross sections this offset is at most a few degrees. The very first

measurements show larger deviations up to about 10° for the $\{\alpha_7\} \rightarrow \{\alpha_5\}$ transition (Fig. 3).

As to the polarization effect, we observe both a qualitatively and quantitatively good agreement between experimental values and quantum results as listed in Table III, certainly in view of the broad energy range accessed by the HCA source. The calculated magnitude of the cross section, however, is mostly larger than the experimentally obtained result (Table III). In view of the estimated systematic error of 22% in the absolute values of the experimental cross sections, these discrepancies are significant. Only for the $\{\alpha_5\} \rightarrow \{\alpha_6, \alpha_9\}$ and $\{\alpha_7\} \rightarrow \{\alpha_4\}$

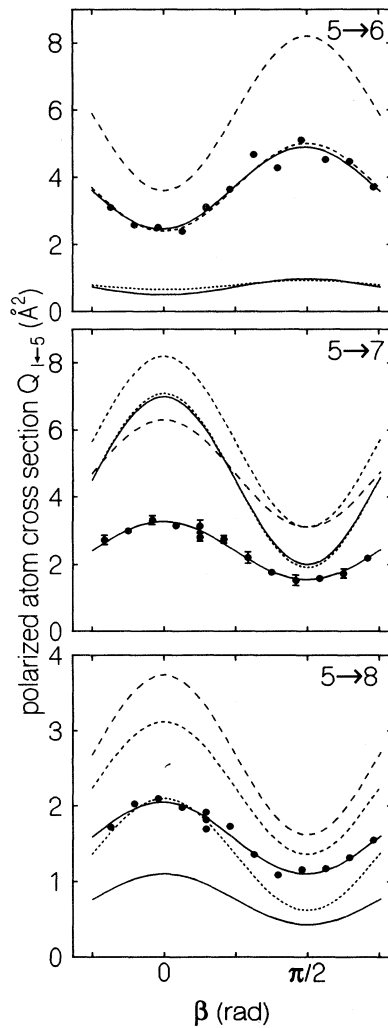


FIG. 2. Experimental results for the observed cross section $Q_{l \leftarrow 5}^\beta$ for the final states $l=6, 7,$ and 8 as a function of the (calculated) angle β between the laser polarization and the relative velocity \mathbf{g} measured at a collision energy $E = 450$ meV. Statistical errors only are indicated. Solid line: least squares fit to data. Second solid line: experimental data [20, 21] for TMS at $E = 100$ meV. Dotted lines: coupled-channel calculations for $E = 100$ meV (.....), 350 meV (- - - -), and 525 meV (- - -).

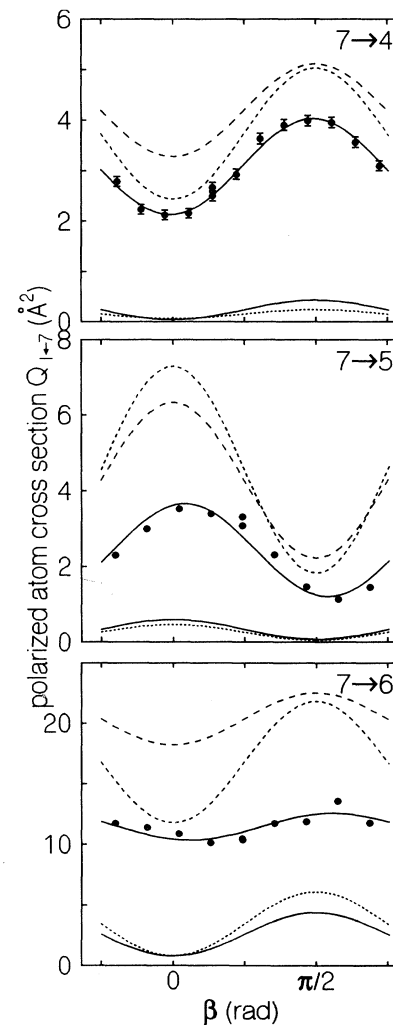


FIG. 3. Experimental results for the observed cross section $Q_{l \leftarrow 7}^\beta$ for the final states $l=4, 5,$ and 6 as a function of β at a collision energy $E = 500$ meV. Statistical errors only are indicated. Solid line: least squares fit to data. Second solid line: experimental data [20, 21] for TMS at $E = 100$ meV. Dotted lines: coupled-channel calculations for $E = 100$ meV (.....), 350 meV (- - - -), and 525 meV (- - -).

transitions is a fair agreement found.

In the TMS case though, mostly an excellent agreement is found for both the polarization effect and cross section magnitude [20,21]. A striking example of the contrast between the TMS and HCA results is the $\{\alpha_5\} \rightarrow \{\alpha_7\}$ transition. Whereas the *thermal* experimental and quantum data closely agree, the corresponding *superthermal* cross sections are wide apart in magnitude by a factor 2. When switching from TMS to HCA source, the rise in magnitude and drop in polarization effect for the $\{\alpha_7\} \rightarrow \{\alpha_4, \alpha_5\}$ transitions clearly reflect the endothermicity of the processes ($\Delta E_{74} = -91$ meV, $\Delta E_{75} = -81$ meV).

B. Initial state $J_k = 2$

For the $\{\alpha_4\}$, $\{\alpha_6\}$, and $\{\alpha_8\}$ initial states with $J_k = 2$, the w_{m_k} distribution is nearly isotropic, apart from the unpopulated $m_k = 0$ level (Table II). The above is reflected in the measurements, with mostly only small values for $\mathcal{P}^{\text{expt}}$ (Table IV). The qualitative agreement with the corresponding quantum values $(\mathcal{P} - \mathcal{Q})^{\text{CC}}$ is good, certainly in view of its magnitude and the differences between the two quantum calculations at different collision energy. Clearly, the use of the anisotropy parameters introduced in this paper shows its value in the comparison between theory and experiment.

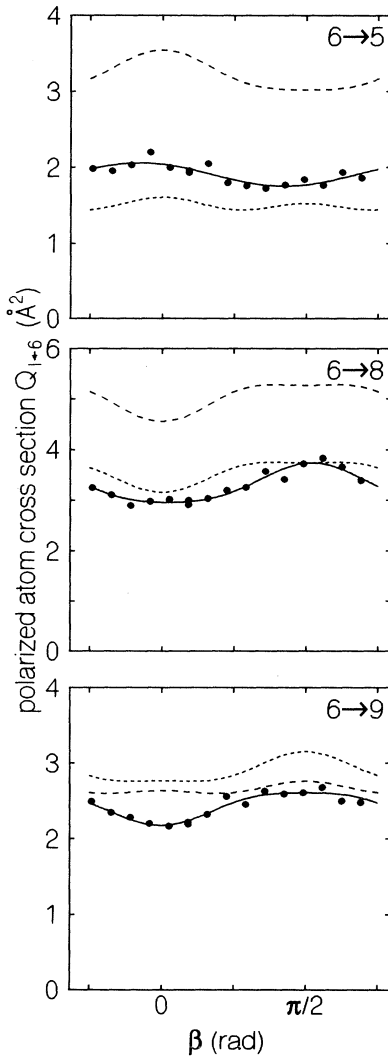


FIG. 4. Experimental results for the cross section $Q_{l \rightarrow 6}^{\beta}$ for the final states $l=5, 8,$ and 9 as a function of β at a collision energy $E = 450$ meV. Statistical errors only are indicated. Solid line: least squares fit to data. Dotted lines: coupled-channel calculations for $E = 350$ meV (---) and 525 meV (- - -).

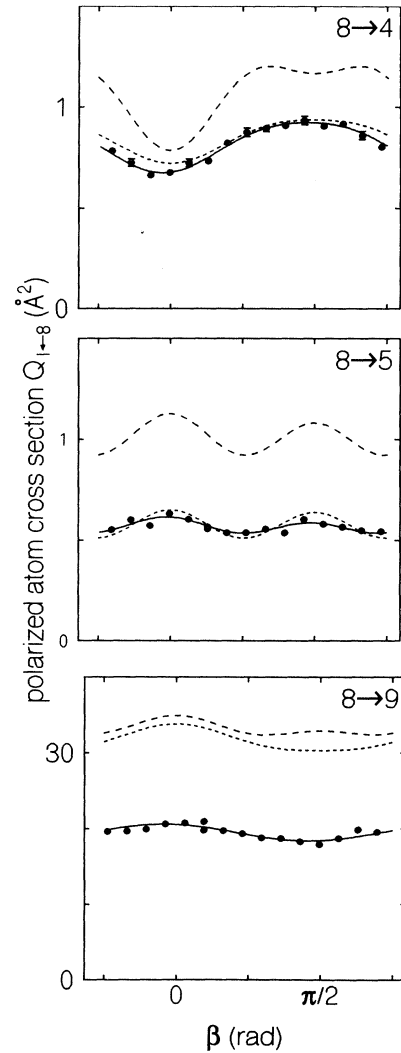


FIG. 5. Experimental results for the cross section $Q_{l \rightarrow 8}^{\beta}$ for the final states $l=4, 5,$ and 9 as a function of β at a collision energy $E = 490$ meV. Statistical errors only are indicated. Solid line: least squares fit to data. Dotted lines: coupled-channel calculations for $E = 350$ meV (---) and 525 meV (- - -).

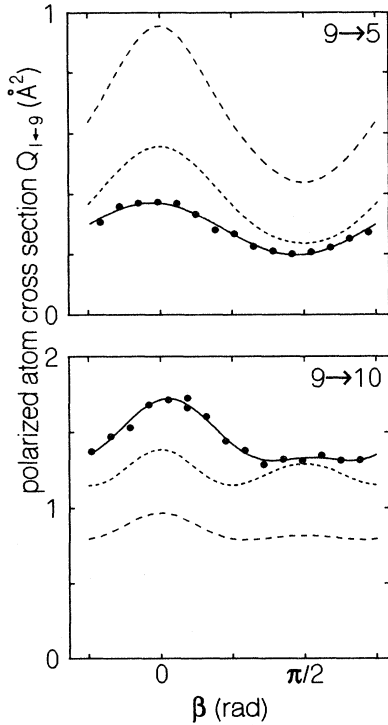


FIG. 6. Experimental results for the cross section $Q_{l \leftarrow 9}^{\beta}$ for the final states $l=5$ and 10 as a function of β at a collision energy $E = 490$ meV. Statistical errors only are indicated. Solid line: least squares fit to data. Dotted lines: coupled-channel calculations for $E = 350$ meV (---) and 525 meV (- - -).

C. Initial state $J_k = 3$

For the $\{\alpha_9\}$ initial state with $J_k = 3$ similar results are obtained, as given in Table V. The $\{\alpha_6\} \rightarrow \{\alpha_5\}$ transition in Fig. 4 is one of the few cases with a cross section

magnitude correctly predicted by quantum calculations. Note that it is only for the case of the $\{\alpha_8\} \rightarrow \{\alpha_{10}\}$ transition (Table IV) and the $\{\alpha_9\} \rightarrow \{\alpha_{10}\}$ transition (Table V) that the quantum calculations result in a lower cross section magnitude than obtained experimentally.

D. Higher order polarization effects

A higher order $\cos(4\beta)$ polarization effect is most clearly observed for the $\{\alpha_9\} \rightarrow \{\alpha_{10}\}$ transition, but is also evidently present for the $\{\alpha_8\} \rightarrow \{\alpha_5, \alpha_4\}$ and $\{\alpha_6\} \rightarrow \{\alpha_8, \alpha_9\}$ transitions. Table VI presents a separate $\cos(4\beta)$ data analysis for these transitions. As can be seen in this table and from the corresponding figures, the qualitative features are in good agreement with the calculations and even the cross section magnitude is correctly predicted. It is only for the $\{\alpha_6\} \rightarrow \{\alpha_8\}$ and $\{\alpha_6\} \rightarrow \{\alpha_9\}$ transitions that the quantum polarization effects seem to be exchanged with respect to each other (Fig. 4). Note that the values for $\mathcal{P}^{\text{expt}}$ of the $\cos(4\beta)$ analysis are consistent with the results of the simple $\cos(2\beta)$ analysis.

E. Detailed balance

Detailed balancing yields

$$E_k (2J_k + 1) Q_{l \leftarrow k}(E_k) = E_l (2J_l + 1) Q_{k \leftarrow l}(E_l) \quad (15)$$

for the unpolarized cross sections of reverse transitions. Here, E_k and E_l are collision energies relative to the k and l level, respectively, corresponding to the same total (kinetic plus electronic) energy. For collision energies much larger than the atomic energy splitting, i.e., $E_k, E_l \gg \Delta E_{kl}$ so that $E_k \simeq E_l$, Eq. (15) states that the ratio of unpolarized cross sections equals the ratio of statistical weights. In Table VII a comparison is made between the unpolarized cross sections for all measured pairs of reverse transitions, ordered by the atomic energy

TABLE VI. Experimental and quantum-mechanical anisotropy parameters \mathcal{P} , \mathcal{Q} and unpolarized cross sections $Q_{l \leftarrow k}$ for various $\{\alpha_k\} \rightarrow \{\alpha_l\}$ transitions with $J_k = 2, 3$. Statistical errors only are indicated. The coupled-channel calculations are referred to as “CC” and are labeled (1) and (2) for collision energies $E_{\text{CC}}=350$ meV and $E_{\text{CC}}=525$ meV, respectively. By the presence of a $\cos(4\beta)$ contribution in the experimental data we are able to determine two experimental anisotropy parameters $\mathcal{P}^{\text{expt}}$, $\mathcal{Q}^{\text{expt}}$, directly comparable to \mathcal{P}^{CC} , \mathcal{Q}^{CC} for $J_k = 2$ or effectively to $(\mathcal{P} + \mathcal{R})^{\text{CC}}$ and $(\mathcal{Q} + \mathcal{R})^{\text{CC}}$ for $J_k = 3$. In the latter case we take $\mathcal{R}^{\text{expt}} = 0$ in the data analysis. Coupled-channel calculations yield $\mathcal{R}_1^{\text{CC}} = -0.56$ and $\mathcal{R}_2^{\text{CC}} = -0.45$, respectively, for $\{\alpha_9\} \rightarrow \{\alpha_{10}\}$ transition.

k	l	E_{expt} (meV)	$Q_{l \leftarrow k}$ (Å ²)	$Q_{l \leftarrow k}^{\text{CC}}/Q_{l \leftarrow k}$		$\mathcal{P}^{\text{expt}}$	\mathcal{P}^{CC}		$\mathcal{Q}^{\text{expt}}$	\mathcal{Q}^{CC}		
				(1)	(2)		(1)	(2)		(1)	(2)	
6	8	450	3.4(2)	1.1	1.5	0.0(2)	0.52	0.44	-0.2(1)	0.34	0.29	
	9	450	2.5(1)	1.2	1.1	0.4(2)	-0.15	-0.17	0.2(1)	-0.26	-0.21	
8	4	490	0.86(3)	1.0	1.3	0.6(1)	0.52	1.33	0.2(1)	0.23	0.91	
	5	490	0.56(3)	1.0	1.8	-0.8(2)	-1.46	-1.17	-0.7(2)	-1.39	-1.08	
							$(\mathcal{P} + \mathcal{R})^{\text{CC}}$				$(\mathcal{Q} + \mathcal{R})^{\text{CC}}$	
9	10	450	1.38(7)	0.9	0.6	0.32(5)	0.47	0.40	0.09(2)	0.18	0.14	

TABLE VII. Evaluation of the detailed balancing requirement for all pairs of measured reversed transitions. For $\Delta E_{kl}=0$ the latter column should yield unity. The large values obtained for the pairs involving the $\{\alpha_9\}$ state point to an underestimation of the cross section magnitude for the $\{\alpha_9\}$ initial state by a factor 2.38. Corrected values are indicated in parentheses.

k	l	ΔE_{kl} (meV)	$(2J_k + 1)Q_{l \leftarrow k} / (2J_l + 1)Q_{k \leftarrow l}$
6	7	24	0.97
5	6	57	1.32
6	8	61	1.51
4	6	67	0.79
5	7	81	1.05
4	7	91	0.75
5	8	118	1.51
4	8	128	1.18
Average value			1.14 ± 0.28
Transitions involving optical excitation in the closed level system ${}^3P_2 \leftrightarrow \{\alpha_9, J_k = 3\}$			
8	9	21	1.61 (0.68)
6	9	82	2.36 (0.99)
5	9	138	2.55 (1.07)
4	9	149	2.99 (1.26)
Average value			$2.38 \pm 0.50 (1.00 \pm 0.21)$

splitting. The average value of the weighted cross section ratio $(2J_k + 1)Q_{l \leftarrow k} / (2J_l + 1)Q_{k \leftarrow l}$ for all transitions not involving the $\{\alpha_9\}$ state is equal to 1.14 ± 0.28 . The values are thus in fair agreement with the requirement of detailed balancing, certainly in view of the estimated systematic error of 22% in the magnitude of the cross section, as discussed in Sec. II B.

For the transitions involving the $\{\alpha_9\}$ state the deviations from detailed balance are rather large. Most likely, this is related to the fact that the $\{\alpha_9\}$ initial state and the 3P_2 level form a closed level system for optical pumping, resulting in a spatially much broader excitation profile. This is also evident from the ratio $Q_{l \leftarrow k}^{CC} / Q_{l \leftarrow k}$, which is significantly higher for the case of an $\{\alpha_9\}$ initial state (Table V) than for the case of an $\{\alpha_9\}$ final state (Tables III and IV). By increasing the magnitude of the $Q_{l \leftarrow 9}$ cross sections by a factor 2.38, which is derived from the average value of the observed weighted cross section ratio for all four transitions, we observe a fair agreement for the detailed balance. The average value and the spread of the weighted cross section ratio then is equal to 1.00 ± 0.21 , in agreement with the estimated systematic errors. The spread is also of the same order of magnitude as found for the other transitions.

F. Thermal energy test on absolute cross sections

To check if the general observation of a too large magnitude of the calculated cross section in comparison with the experimental values is due to changes in the setup when switching from TMS to HCA source, the $\{\alpha_5\} \rightarrow \{\alpha_4\}$ transition is remeasured with the TMS

positioned in the HCA chamber. Usually, the TMS is exchanged with the defining aperture (Fig. 1). Because of its cross section magnitude this transition is ideally suited as a reference. A convolution factor $\xi=0.90$ is determined for this transition with the TMS. In Fig. 7 our experimental results are compared with previous measurements [21]. Agreement is found to be within 10%. Clearly the setup used and the beam alignment are of no importance for the magnitude of the measured cross section.

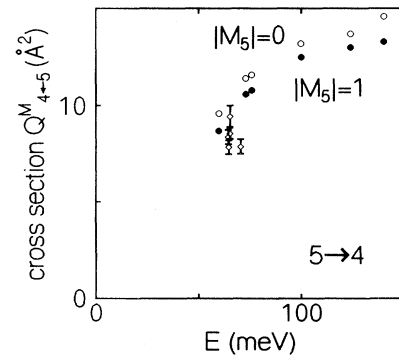


FIG. 7. Comparison between experimentally determined cross sections for the $\{\alpha_5\} \rightarrow \{\alpha_4\}$ transition. The values obtained for the TMS in the HCA chamber agree well with those previously reported [21] with the TMS only $L=90$ mm from the scattering center. This excludes a systematic difference in the determination of the cross section magnitude.

V. FAILING SEMICLASSICAL MODEL

Due to the “black box” character of the coupled-channel calculation it is difficult to determine the nature of the observed discrepancies between experimental and quantum cross section magnitudes. In the semiclassical model the link between model potentials and cross sections is a far more direct one. A qualitative semiclassical interpretation of the data is therefore helpful in this context. As we will see in this section, however, the current semiclassical model fails in describing important features of the data.

In the current semiclassical model [21] transitions are only possible at localized avoided crossings in the adiabatic potentials, referred to as *radial coupling*. The single-pass transition probability p_{kl} involving the adiabatic k and l states is given by the Landau-Zener formula [30]

$$p_{kl} = \exp(-v_{kl}/v_{\text{rad}}), \quad (16)$$

$$v_{kl} = 2\pi(H_{kl})^2/\hbar\Delta F,$$

in which v_{rad} is the local radial velocity. The reference

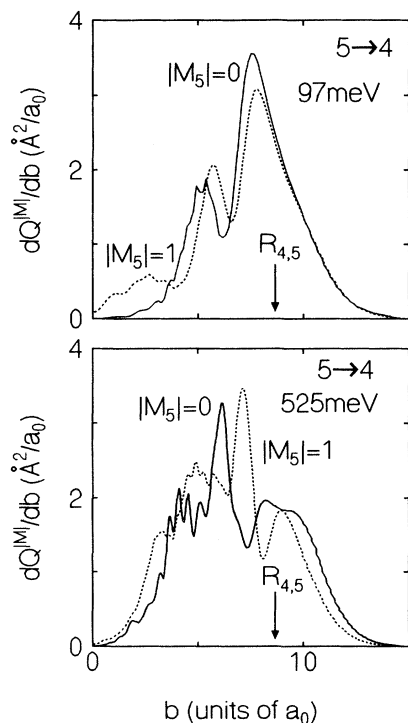


FIG. 8. Quantum-mechanical differential cross sections $dQ_{4\leftarrow 5}^{M_5}/db$ as a function of the impact parameter b for both collision energies $E = 97$ meV and $E = 525$ meV, with an averaging applied over three and five values, respectively, of the quantum number for the total angular momentum. The arrow points to the position R_x of the avoided crossing. Both the contribution for impact parameters $b > R_x$ and the rise in magnitude for $b < R_x$ going to HCA energy cannot be explained by the current semiclassical model.

velocity v_{kl} characterizes the avoided crossing, with $2H_{kl}$ the energy splitting between the adiabatic curves at the crossing radius R_x and ΔF the absolute difference in the slopes of the corresponding local diabatic potential curves. A net transition is most likely to occur when $v_{\text{rad}} \approx v_{kl}$ and a change in adiabatic potential is made only once, either on the incoming or the outgoing transit.

The other major ingredient of the semiclassical model is the locking concept. For internuclear distances R smaller than the so-called locking radius $R_L \approx 7a_0$ the molecular interaction forces are large enough to “lock” \mathbf{J} to the internuclear axis. For $R > R_L$ the \mathbf{J} vector remains space fixed. This implies a redistribution over the different Ω states along the trajectory, known as *rotational coupling*. Note that this redistribution is purely determined by geometry, i.e., by the space-fixed orientation of \mathbf{J} and the followed trajectory, and in a first approximation not by the magnitude of \mathbf{g} for a fixed value of R_L [31].

A. $\{\alpha_5\} \rightarrow \{\alpha_4\}$ transition

The $\{\alpha_5\} \rightarrow \{\alpha_4\}$ transition is due to an avoided crossing in the $\Omega=1$ manifold at $R_x = 8.6a_0$, as is obvious from an inspection of the potential curves involved [1, 2, 20, 21]. The very low reference velocity $v_{45}=20$ m/s implies $p_{45} \approx 1$. A net transition occurs only when the crossing is met once along a full trajectory. Rotational coupling between R_x and R_L is required to prevent a second transit of the crossing by converting $\Omega = 1$ components into $\Omega \neq 1$ components and vice versa. Since both p_{45} and the rotational coupling only slightly depend on g , more or less equal cross sections for the TMS and the HCA source are expected. This is indeed seen for both the experimental and quantum results. However, a closer look at the quantum results reveals an inconsistent feature. In Fig. 8 the quantum-mechanical partial cross section $dQ_{4\leftarrow 5}^{M_5}/db$ is given as a function of the impact parameter b . An averaging procedure is applied to remove the fast Stückelberg oscillations. Going from TMS to HCA energy, two effects are apparent: a clear rise in dQ/db for $b < R_x$ and a counteracting drop for $b > R_x$. The rise for $b < R_x$ contradicts the semiclassical view depicted above. The long-range dQ/db contributions for $b > R_x$ were mentioned before [21] and are also not explained in the current semiclassical model, since the crossing simply cannot be reached.

B. $\{\alpha_6\} \rightarrow \{\alpha_7\}$ transition

The (67) avoided crossing in the $\Omega=1$ manifold resembles the (54) crossing [1, 2, 20, 21], also having a small reference velocity $v_{67}=165$ m/s [21]. An essential difference is the smaller crossing radius $R_x = 7.35a_0$ [21]. With $R_x \approx R_L$, the crossing is bound to be passed twice. With increasing energy, p_{67} approaches unity and we expect a clear drop in cross section magnitude at HCA energy. This is fully contradicted by both the experiment and the quantum calculations, showing a clear increase for both the $\{\alpha_7\} \rightarrow \{\alpha_6\}$ and the $\{\alpha_6\} \rightarrow \{\alpha_7\}$ transition. At TMS energy the quantum differential cross section $dQ_{6\leftarrow 7}^{M_7}/db$ (Fig. 9) displays a maximum at $b \approx 5a_0 < R_x$,

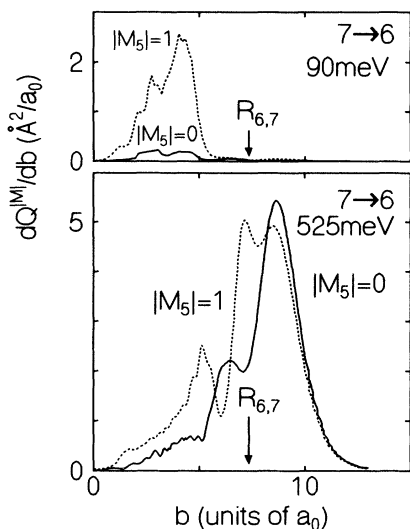


FIG. 9. Quantum-mechanical differential cross sections $dQ_{6←7}^{M7}/db$ for both $E = 90$ meV and $E = 525$ meV. See caption of Fig. (8) for further detail. At HCA energy, the major part of the cross section stems from large impact parameter contributions unexplained by the current semiclassical model.

where the radial velocity at the crossing is minimal. At HCA energy we see that the main part of the cross section is due to impact parameters $b > R_x$ for which the crossing cannot be reached. For the reverse transition a similar result is obtained. Clearly, the yet unexplained long-range dQ/db contributions are no longer uniquely reserved for the $\{\alpha_5\} \rightarrow \{\alpha_4\}$ transition, as is the case at TMS energy.

C. $\{\alpha_8\} \rightarrow \{\alpha_9\}$ transition

To explain the transitions involving $\{\alpha_8\}$ and $\{\alpha_9\}$ states new avoided crossings have to be identified. However, these are not as evidently present as the crossings in the (4567) group. Consequently, relatively large values for H_{kl} are to be found, implying large reference velocities. An interesting case now are the $\{\alpha_9\} \leftrightarrow \{\alpha_8\}$ transitions. Though not depicted here, these also exhibit a major contribution at large impact parameters. We conclude that the value of the reference velocity is not related to the presence of long-range dQ/db contributions. The similarity between the results for the $\{\alpha_4, \alpha_5, \alpha_6\} \rightarrow \{\alpha_8\}$ and the $\{\alpha_4, \alpha_5, \alpha_6\} \rightarrow \{\alpha_9\}$ transitions and the relatively large cross section found for the $\{\alpha_9\} \leftrightarrow \{\alpha_8\}$ transitions imply a strong coupling of the $\{\alpha_8\}$ and $\{\alpha_9\}$ states in the collision process.

VI. RADIAL MATCHING

With the HCA source the largest cross sections are measured for the $\{\alpha_9\} \leftrightarrow \{\alpha_8\}$, $\{\alpha_7\} \leftrightarrow \{\alpha_6\}$, and $\{\alpha_5\} \rightarrow \{\alpha_4\}$ transitions. Common features of these transitions are the relatively small atomic energy splittings $\Delta E_{45}=10.7$ meV, $\Delta E_{67}=24.1$ meV, and $\Delta E_{89}=20.7$

meV, the small experimental polarization effect (observed both experimentally as well as quantum mechanically) and the fact that they all show pronounced long-range dQ/db contributions in the calculations. Though minorly contributing, long-range dQ/db contributions are also evidently present for the $\{\alpha_5\} \leftrightarrow \{\alpha_6\}$, $\{\alpha_6\} \leftrightarrow \{\alpha_8\}$, and $\{\alpha_7\} \leftrightarrow \{\alpha_8\}$ transitions.

We conclude that essentially a long-range transition mechanism has to be added to the current semiclassical model. Possibly such a mechanism can be related to the broad and low amplitude structures of the radial coupling matrix elements $\langle \alpha_l | (\partial/\partial R) | \alpha_k \rangle^{\Omega}$ at large internuclear distances, instead of the peaked structures in the inner region that correspond to localized avoided crossings [21]. An important question is how kinetic energy can be transferred to electronic potential energy at these large internuclear distances. Clearly this is not by a change in the radial kinetic energy, since the potentials are small in magnitude and vary only slowly for large R , so that only small radial forces are involved. As for the rotational energy, however, a change in the rotational quantum number N can bridge the electronic energy difference. In Fig. 10 the quantum-mechanical differential cross section $dQ_{6←7}^{\Delta N}/db$ for the possible (even) changes

$$\Delta N = N_6 - N_7 \quad (17)$$

of N are depicted for a collision energy $E=1000$ meV. We observe a major cross section contribution at large impact parameters $b > R_x$, with a clear preference for $\Delta N = -2$. This is exactly what we expect from the above argument. A decrease in N for the final $\{\alpha_6\}$ state, which lies *above* the initial $\{\alpha_7\}$ state, is effective in surmounting the endothermic energy barrier $\Delta E_{6,7} = 24$ meV. In quantum-mechanical terms the transition can qualitatively be described in the distorted wave approximation by two radial wave functions for a different $\{\alpha, N\}$ combination that “match” in wavelength, i.e., have the same radial kinetic energy, over a certain R range, with

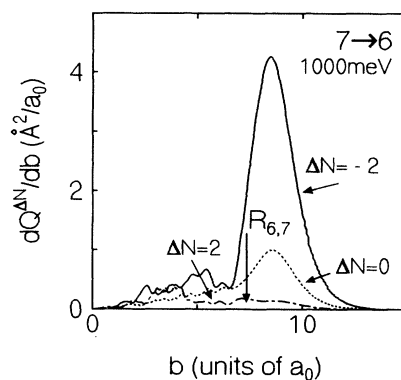


FIG. 10. Quantum-mechanical differential cross sections $dQ_{6←7}^{\Delta N}/db$ as a function of the impact parameter b for $E = 1000$ meV. A clear preference for $\Delta N = N_6 - N_7 = -2$ is observed, in favor of the discussed “radial matching” mechanism.

a small and slowly varying nondiagonal matrix element coupling the two. Semiclassically we find a scaling

$$\begin{aligned}\Delta E_{\text{rot}} &= E_{\text{rot}}(N + \Delta N) - E_{\text{rot}}(N) \\ &= \Delta N(N + \frac{1}{2})\hbar^2/\mu R^2 \approx \Delta N\hbar gb/R^2,\end{aligned}\quad (18)$$

with b the impact parameter and μ the reduced mass. Because $\Delta E_{\text{rot}} \sim g$ it is clear that larger energy differences can be bridged at HCA energy, resulting in more cases with long-range dQ/db contributions than only the $\{\alpha_5\} \rightarrow \{\alpha_4\}$ case at TMS energy.

This also points to a possible explanation of the observed differences in the magnitude of the cross section for the experimental and the quantum results, i.e., a possible deficiency in the long-range part of the model potentials. This has to be investigated in more detail. Note the counterintuitive idea of a transition at higher collision energy being more sensitive to the details of the long-range potential instead of the repulsive branch.

VII. CONCLUDING REMARKS

In this paper the experimental cross sections are reported for the process of intramultiplet mixing in the $\text{Ne}^{**}\text{-He}$ system at superthermal energies. A broad range of cross section magnitudes and polarization effects is observed. Although the polarization effects are in good agreement with quantum coupled-channel calculations, the calculated values for the cross section magnitude are

mostly too large. Furthermore, the most prominent experimental cross sections cannot be explained by the current semiclassical model. Although a scaling problem is highly unlikely, time-of-flight measurements on the energy dependence of the cross section [31] provide even more definite experimental evidence for a shortcoming in the current semiclassical model. A first attempt is made to identify the additional transition mechanism involved. The radial matching mechanism is a prime candidate. In that case the long-range part of the potential strongly influences the cross section magnitude, whereas polarization effects are governed by the avoided crossings in the inner region. A new semiclassical model incorporating this effect is in development. A useful tool in this is the comparison between semiclassical and quantum-mechanical partial cross sections. Ultimately, a fast numerical implementation of such a semiclassical model should allow a reconstruction of the model potentials, given the extensive size of the set of available cross sections. Moreover, the time-of-flight measurements on the velocity dependency of the cross sections [31] will also be included in this analysis.

A final prospect is to reveal possible differences in $^{20}\text{Ne}^{**}\text{-}^{(20)}\text{Ne}$ and $^{22}\text{Ne}^{**}\text{-}^{(20)}\text{Ne}$ cross sections due to symmetry effects [32], where the notation $^{(20)}\text{Ne}$ is used for the natural isotope mixture of neon with 90% of ^{20}Ne . These are likely to appear at the shorter internuclear distances probed with the HCA source. As yet, these measurements have not been carried out.

-
- [1] D. Hennecart, Ph.D. thesis, Université de Caen, Caen, France, 1982 (unpublished).
 - [2] D. Hennecart and F. Masnou-Seeuws, *J. Phys. B* **18**, 657 (1985).
 - [3] E.E.B. Campbell, H. Schmidt, and I.V. Hertel, *Adv. Chem. Phys.* **72**, 37 (1988).
 - [4] C.T. Rettner and R.N. Zare, *J. Chem. Phys.* **75**, 3636 (1981); **77**, 2416 (1982).
 - [5] J.M. Mestdagh, J. Berlande, P. de Pujo, J. Cuvellier, and A. Biner, *Z. Phys. A* **304**, 3 (1982).
 - [6] J.P. Visticot, P. de Pujo, O. Sublemontier, A.J. Bell, J. Berlande, J. Cuvellier, T. Gustavsson, A. Lallement, J.M. Mestdagh, P. Meynadier, and A.G. Suits, *Phys. Rev. A* **45**, 6371 (1992).
 - [7] R. Düren, E. Hasselbrink, and H. Tischer, *Phys. Rev. Lett.* **50**, 1983 (1983).
 - [8] R. Düren and E. Hasselbrink, *J. Chem. Phys.* **85**, 1880 (1986).
 - [9] W. Bussert, T. Bregel, R.J. Allan, M.W. Ruf, and H. Hotop, *Z. Phys. A* **320**, 105 (1985).
 - [10] W. Bussert, D. Neuschäfer, and S.R. Leone, *J. Chem. Phys.* **87**, 3833 (1987).
 - [11] E.E.B. Campbell, H. Hülser, R. Witte, and I.V. Hertel, *Z. Phys. D* **16**, 21 (1990).
 - [12] H.A.J. Meijer, *Z. Phys. D* **17**, 257 (1990).
 - [13] A.G. Suits, H.T. Hou, and Y.T. Lee, *J. Phys. Chem.* **94**, 5672 (1990).
 - [14] R.L. Robinson, L.J. Kovalenko, C.J. Smith, and S.R. Leone, *J. Chem. Phys.* **92**, 5260 (1990).
 - [15] J.P.J. Driessen, C.J. Smith, and S.R. Leone, *Phys. Rev. A* **44**, 1431 (1990); *J. Phys. Chem.* **95**, 8163 (1990).
 - [16] R.L. Dubs, P.S. Julienne, and F.H. Mies, *J. Chem. Phys.* **93**, 8784 (1990).
 - [17] M.P.I. Manders, J.P.J. Driessen, H.C.W. Beijerinck, and B.J. Verhaar, *Phys. Rev. Lett.* **57**, 1577 (1986); **57**, 2472 (1986).
 - [18] M.P.I. Manders, W.M.J. Ruyten, F.v.d. Beucken, J.P.J. Driessen, W.J.T. Veugelers, P.H. Kramer, E.J.D. Vredendregt, W.B.M. van Hoek, G.J. Sandker, H.C.W. Beijerinck, and B.J. Verhaar, *J. Chem. Phys.* **89**, 4777 (1988).
 - [19] H.C.W. Beijerinck, G.H. Kaashoek, J.P.M. Beijers, and M.J. Verheijen, *Physica B+C* **121C**, 425 (1983).
 - [20] M.P.I. Manders, J.P.J. Driessen, H.C.W. Beijerinck, and B.J. Verhaar, *Phys. Rev. A* **37**, 3237 (1988).
 - [21] M.P.I. Manders, W.B.M. van Hoek, E.J.D. Vredendregt, G.J. Sandker, H.C.W. Beijerinck, and B.J. Verhaar, *Phys. Rev. A* **39**, 4467 (1989).
 - [22] P.G.A. Theuws, H.C.W. Beijerinck, D.C. Schram, and N.F. Verster, *J. Phys. E* **15**, 573 (1982); P.G.A. Theuws, Ph.D. thesis, Eindhoven University of Technology, Eindhoven, 1981 (unpublished).
 - [23] M.J. Verheijen, H.C.W. Beijerinck, L.H.A.M. van Moll, J. Driessen, and N.F. Verster, *J. Phys. E* **17**, 904 (1984).
 - [24] W. Bussert, T. Bregel, R.J. Allan, M.W. Ruf, and H. Hotop, *Z. Phys. A* **320**, 105 (1985).
 - [25] J.P.J. Driessen, F.J.M. van de Weijer, M.J. Zonneveld, L.M.T. Somers, M.F.M. Janssens, H.C.W. Beijerinck, and B.J. Verhaar, *Phys. Rev. Lett.* **62**, 2369 (1989); *Phys. Rev. A* **42**, 4058 (1990).
 - [26] J.S. Cohen and B. Schneider, *J. Chem. Phys.* **61**, 3230

- (1974).
- [27] W. Boom, Ph.D. thesis, Eindhoven University of Technology, 1993.
- [28] S.S. Op de Beek, Eindhoven University of Technology Report No. VDF/NO 92-18, 1992 (unpublished).
- [29] A. Messiah, *Quantum Mechanics* (North-Holland, Amsterdam, 1981), Vols. I and II.
- [30] E.E. Nikitin, in *Chemische Elementar Prozesse*, edited by H. Hartmann and J. Heidelberg (Springer-Verlag, Berlin, 1968).
- [31] W. Boom, S.S. Op de Beek, R.A.M.L. van Galen, F.J.J. Huijsmans, H.C.W. Beijerinck, and B.J. Verhaar, *Phys. Rev. A* **49**, 4660 (1994).
- [32] M.P.I. Manders, W. Boom, H.C.W. Beijerinck, and B.J. Verhaar, *Phys. Rev. A* **39**, 5021 (1989).